Surface Defects Enhanced Visible Light Photocatalytic H_2 Production for Zn-Cd-S Solid Solution

*Xiaoyan Zhang, Zhao Zhao, Wanwan Zhang, Guoqiang Zhang, Dan Qu, Xiang Miao, Shaorui Sun, and Zaicheng Sun**

In order to investigate the defect effect on photocatalytic performance of the visible light photocatalyst, Zn-Cd-S solid solution with surface defects is prepared in the hydrazine hydrate. X-ray photoelectron spectra and photoluminescence results confirm the existence of defects, such as sulfur vacancies, interstitial metal, and Zn and Cd in the low valence state on the top surface of solid solutions. The surface defects can be effectively removed by treating with sulfur vapor. The solid solution with surface defect exhibits a narrower band gap, wider light absorption range, and better photocatalytic perfomance. The optimized solid solution with defects exhibits 571 μmol h^{-1} *for 50 mg photocatalyst without loading Pt as cocatalyst under visible light irradiation, which is fourfold better than that of sulfur vapor treated samples. The wavelength dependence of photocatalytic activity discloses that the enhancement happens at each wavelength within the whole absorption range. The theoretical calculation shows that the surface defects induce the conduction band minimum and valence band maximum shift downward and upward, respectively. This constructs a type I junction between bulk and surface of solid solution, which promotes the migration of photogenerated charges toward the surface of nanostructure and leads to enhanced photocatalytic activity. Thus a new method to construct highly efficient visible light photocatalysts is opened.*

1. Introduction

Solar-driven production of hydrogen (H_2) from water splitting is considered as one of the promising ways to provide clean fuels.[1] There are two critical issues for high efficient photocatalytic solar energy conversion. One is the extension of light absorption into visible light region, and the other is the enhancement of quantum efficiency at each wavelength.[2] In the former case, the light absorption band strongly depends on the intrinsic band gap of the photocatalyst materials. Regarding to the latter case, enhancement of quantum efficiency has been attempted by improving the methods of modification and synthesis. It is believed that the recombination of photogenerated electrons and holes is one of the most critical factors to depressing the photocatalytic activity, and lattice defects may work as the recombination

---

X. Zhang, Z. Zhao, G. Zhang, D. Qu, X. Miao,
Prof. Z. Sun
State key Laboratory of Luminescence and
Applications
Changchun Institute of Optics
Fine Mechanics and Physics
CAS 3888 East Nanhu Road, Changchun
Jilin 130033, P. R. China
E-mail: sunzc@bjut.edu.cn

X. Zhang, Z. Zhao, G. Zhang, D. Qu, X. Miao
University of Chinese Academy of Sciences
Beijing 100049, P. R. China

W. Zhang, Prof. S. Sun, Prof. Z. Sun
Beijing Key Laboratory of Green Catalysis and Separation
Department of Chemistry and Chemical Engineering
Beijing University of Technology
100 Pingleyuan, Beijing 100124, P. R. China

DOI: 10.1002/smll.201503067

center.[3] However, a few reports have demonstrated that the photocatalytic activity can be improved by introducing defects into photocatalyst materials within a certain concentration.[4] Takata and Domen demonstrated that doping of a cation with valence lower than that of the parent cation effectively enhanced photocatalytic activity.[2] Later, Ti^{3+} doped TiO_2 nanocrystals display an enhanced photocatalytic performance and enhanced IPCE.[5,6] On the other hand, oxides nanocrystals (TiO_2, $SrTiO_3$) with surface oxygen vacancies are prepared by chemical reduction treatment at mild temperature.[6] It is reported that oxygen vacancies induce an enhanced photoexcited electrons and holes separation, which is beneficial to the photocatalytic performance of oxides. Liu and co-workers reported that N vacancies could also promote the photocatalytic activity of g-C_3N_4.[7]

Although many research works have been demonstrated that defects can enhance their photocatalytic performance for the oxide photocatalyst, such as TiO_2 and $SrTiO_3$, due to excellent charge separation efficiency within their whole absorption band. Normally, oxides have large band gap (>3.0 eV) and only absorb UV light. It is expected that the high efficient charge separation will greatly promote the visible light photocatalytic performance if the defects are introduced into the visible light photocatalyst. However, few reports focus on the effect of defects on the photocatalytic activity of visible light photocatalyst, like sulfides, which have an extended visible light absorption from UV to visible light region (≈550 nm).[8] On the other hand, it is noteworthy that avoiding the usage of Pt cocatalyst is highly desired from a practical point of view for the application of photocatalytic H_2 production.[9,10] Zn-Cd-S solid solutions are extensively investigated chalcogenide photocatalyst with visible light response and without using Pt as cocatalyst for water splitting H_2 production.

In this context, we successfully demonstrate that Zn-Cd-S solid solution with surface defects exhibits an enhanced photocatalytic activity within the whole visible light response region by constructing a type I junction. A series of Zn-Cd-S solid solutions were prepared in hydrazine hydrate through hydrothermal route. Photoluminescence (PL) and X-ray photoelectron spectra (XPS) results confirm the existence of surface defects, such as sulfur vacancies, interstitial metal, and Zn and Cd in the low valence state on the surface of solid solution nanostructures. Furthermore, the surface defects could be removed by the sulfur vapor treatment. The wavelength dependence of photocatalytic H_2 production rate demonstrates that the Zn-Cd-S solid solution with surface defects have higher H_2 evolution rate at each wavelength within the whole absorption band. The optimized sample exhibits high visible-light photocatalytic H_2 production rate, which reaches 571 μmol h^{-1} for 50 mg photocatalyst under visible light irradiation ($\lambda > 420$ nm). That is about four times better than that of Zn-Cd-S solid solution with the absence of surface defects (140 μmol h^{-1}). Theoretical calculation demonstrates defect bands could appear at below CB and above VB of solid solution. A type I junction is built up between bulk solid solution and surface layer, which promotes the photogenerated charges migrate toward surface of nanostructures. These are beneficial to the whole photocatalysis process and enhance the overall photocatalytic performance of the Zn-Cd-S solid solutions.

2. Results and Discussions

2.1. Crystalline Phase and Morphology

In order to prepare the solid solution with defects, Zn-Cd-S solid solutions are prepared through the hydrothermal reaction in reduction media hydrazine hydrate as solvent. According to the feed molar ratio of Zn and Cd content, we denote the sample as Zn_mCd_n (m, n = 0–8), where m and n are the feeding molar ratio of Zn and Cd, respectively. **Figure 1** shows X-ray diffraction (XRD) patterns of as-prepared Zn-Cd-S solid solutions. It can be seen that the diffraction peaks of Zn_0Cd_8 sample are well indexed as hexagonal wurtzite CdS (JCPDS Card No. 41-1049). When a small amount of Zn is added into, the diffraction peaks show a slight shift toward the high angle in Zn_1Cd_7 sample. That implies that Zn^{2+} incorporates into the lattice of CdS crystal and decreases the fringe lattice distance of CdS crystal due to the smaller radius of Zn^{2+} (0.74 Å) than that of Cd^{2+} (0.97 Å). With further increasing the Zn content in the reaction, the XRD peaks continuously shift to the high angle side. That also indicates that the as-prepared samples are solid solutions, not mixture of ZnS and CdS. From other side, the Zn_8Cd_0 sample also displays a typical diffraction pattern of hexagonal wurtzite ZnS (JCPDS Card No. 36-1450). The XRD diffraction peaks continuously shift to the low angle with increasing the content of Cd owing to large radius of Cd. The samples, like Zn_5Cd_3 and Zn_4Cd_4, clearly show two groups of diffraction peaks located between the corresponding diffraction peaks of CdS and ZnS. One is close to the crystal phase of wurtzite CdS, the other is similar as the crystal phase of wurtize ZnS. We infer that the as-prepared samples may contain two kinds of Zn-Cd-S solid solutions.

Furthermore, the morphology of Zn-Cd-S solid solutions (Zn_mCd_n) is characterized by scanning electron microscopy

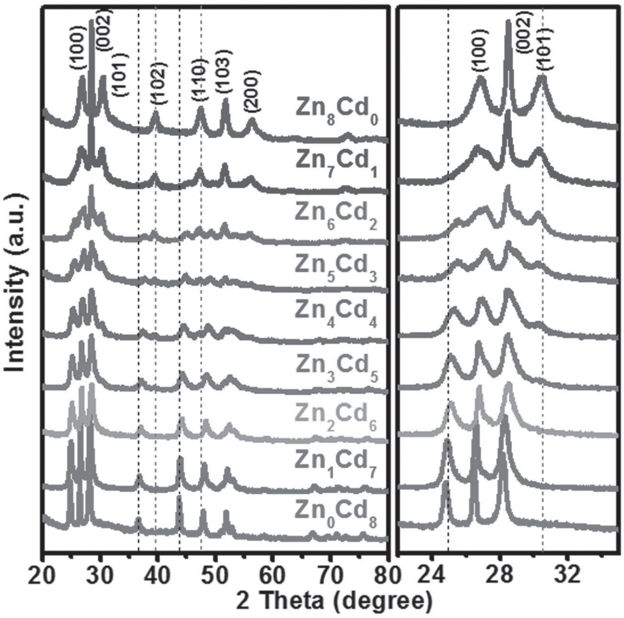

Figure 1. Powder X-ray diffraction of Zn-Cd-S solid solutions with different Zn/Cd ratio (Zn_mCd_n, where m and n are the molar ratio of Zn and Cd feeding amount).

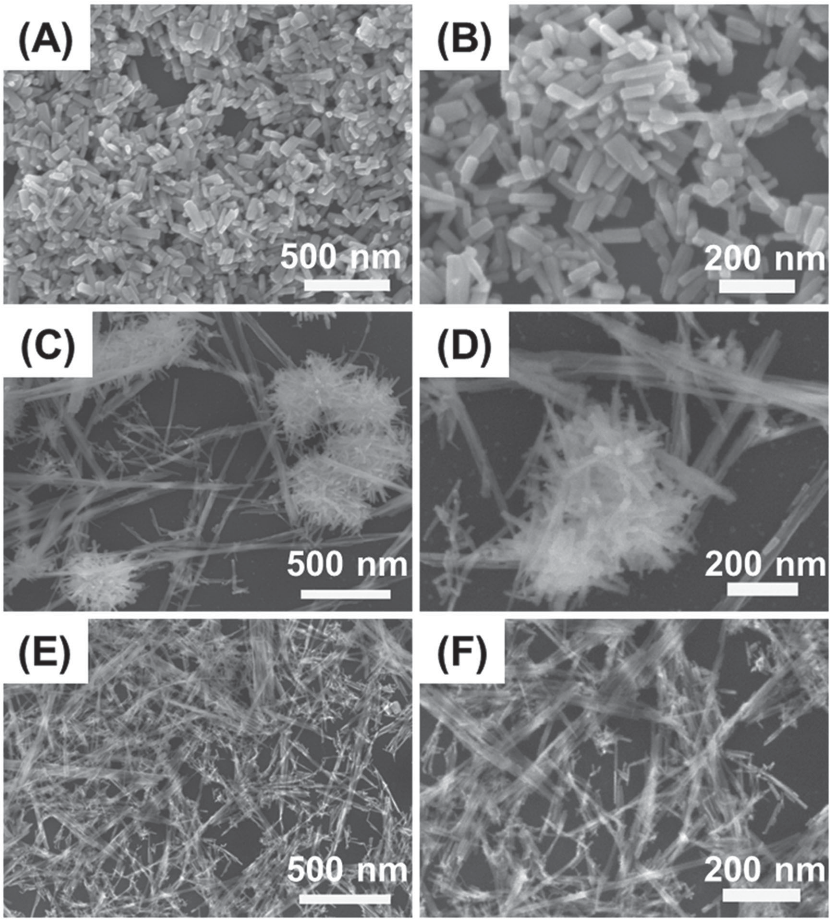

Figure 2. Scanning electron microscopy (SEM) images of Zn-Cd-S solid solutions. A,B) Zn_0Cd_8 (CdS), C,D) Zn_4Cd_4, E,F) Zn_8Cd_0.

(SEM) and shown in **Figure 2** and Figure S1 of the Supporting Information. Zn_0Cd_8 (CdS) clearly shows uniform nanorod structure with ≈120 nm in length and ≈40 nm in width. In the case of Zn_1Cd_7 sample (Figure S1, Supporting Information), the spheres composed of nanorods are also observed besides individual nanorods. The nanorod aggregates take the dominated morphology in the Zn_2Cd_6 sample with the increase of Zn content. The nanowire bundles and nanorod aggregates are observed in the Zn_3Cd_5 sample. With further increasing the feeding amount of Zn, the nanorod aggregates and nanowire bundles coexist in the as-prepared samples (Zn_3Cd_5–Zn_6Cd_2 samples in Figure S1, Supporting Information). The nanowire bundles become the majority in the Zn_7Cd_1 and finally turn pure nanowire bundles for the Zn_8Cd_0 sample (ZnS Figure 2E,F). These results are well agreement with the XRD results, which the as-prepared samples are the mixtures of two morphologies of solid solutions. The formation process of solid solution was investigated by tracking the reaction (see Figures S2–S6, Supporting Information).

2.2. The Composition of Solid Solutions

In order to discover the composition of nanorod aggregates and nanowire bundles, transmission electron microscopy (TEM) and selective area EDAX were further employed to characterize the crystalline phase and composition of Zn_4Cd_4 sample. **Figure 3**A exhibits the TEM image of the nanorod aggregates with ≈1.3 μm in diameter, which is composed with nanorods with ≈10 nm in width. High resolution TEM (HR-TEM) displays the individual nanorod with highly crystalline nature. The lattice fringe with *d* spacing of ≈0.345 nm is close to the (100) lattice plane of hexangonal CdS. The selected area EDAX spectrum (Figure 3B) on the nanorod aggregates discloses that the Zn, Cd, and S exist in the nanorod aggregates. The element composition of nanorod aggregates is $Zn_{0.31}Cd_{0.69}S_{0.77}$, indicating that the content of Cd is higher than Zn content in the nanorod aggregates. It should be noted that sulfur content is stoichiometric deficiency in the nanorod aggregates. Furthermore, the TEM images of nanowire bundles component, as shown in Figure 3C, also exhibit highly crystalline nature with lattice fringe of 0.330 nm, which is close to the (100) lattice plan of hexagonal ZnS. The selected area EDAX spectrum (Figure 3D) also displays the coexistence of Zn, Cd, and S. However, the composition of nanowire bundles is close to $Zn_{0.78}Cd_{0.22}S_{0.78}$, which has higher Zn content in solid solution. These results further confirm that the composition of these two kinds of Zn-Cd-S solid solutions is different. The nanorod aggregates possess higher Cd content ($Zn_{0.31}Cd_{0.69}S_{0.77}$) and the nanowire bundles have higher Zn content. These results are consistence with the XRD and SEM results. In addition, both Zn-Cd-S solid solutions are sulfur deficiency, indicating the existence of sulfur vacancies in the sample.

2.3. The Photoluminescence Spectra

PL spectra of Zn_mCd_n under excitation of 325 nm laser are shown in **Figure 4**. In the PL spectrum of Zn_8Cd_0 (ZnS) sample, it can be fitted into 3 emission bands at ≈410, ≈480, and ≈560 nm. Wang et al detailed investigated the various PL band originated from different defects, such as surface states, sulfur vacancies, zinc vacancies, and interstitial zinc. The blue emission (430 nm) is assigned to surface states of ZnS, while the green (515 nm) and orange (620 nm) emission bands are attributed to the electron transfer from sulfur vacancy to interstitial sulfur states and recombination between interstitial zinc states and zinc vacancies.[11] In our studies, the emission band at 410 nm is attributed to the surface states of ZnS nanocrystals, as well. Zinc vacancies hardly exist due to the deficiency of S according to EDAX and XPS results. Both the cyan (480 nm) and green (560 nm) emissions in our cases

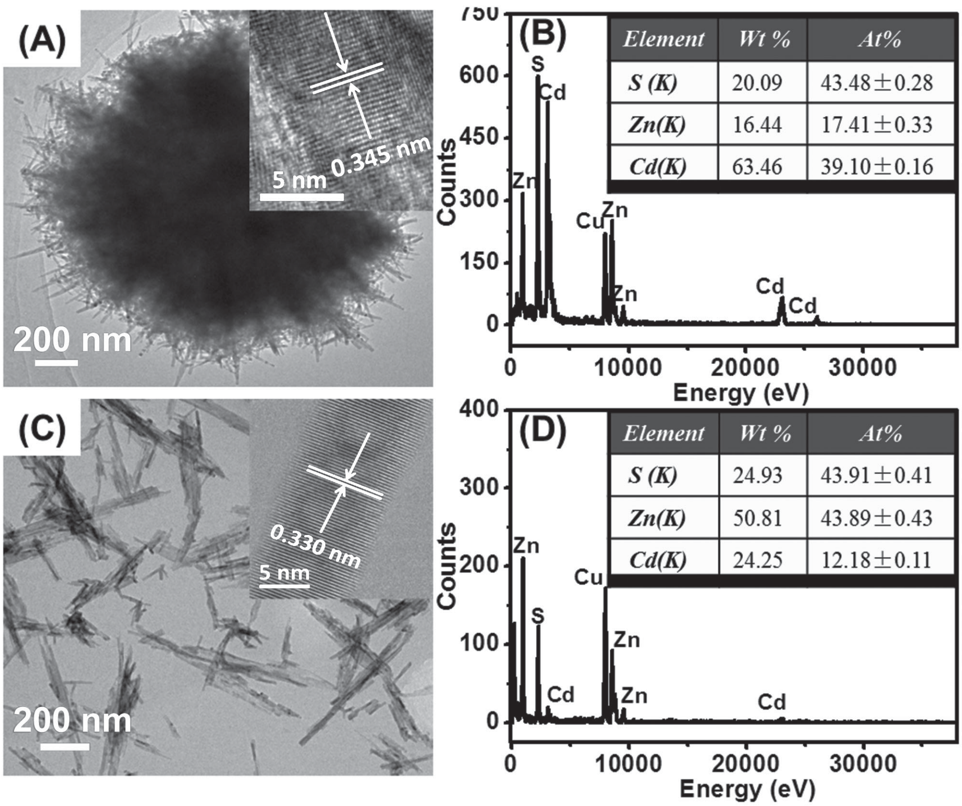

Element	*Wt %*	*At%*
S (K)	20.09	43.48±0.28
Zn(K)	16.44	17.41±0.33
Cd(K)	63.46	39.10±0.16

Element	*Wt %*	*At%*
S (K)	24.93	43.91±0.41
Zn(K)	50.81	43.89±0.43
Cd(K)	24.25	12.18±0.11

Figure 3. Transmission electron microscopy (TEM) images of Zn-Cd-S solid solution (Zn_4Cd_4). A) nanorod aggregates, B) EDAX spectrum of nanorod aggregates, C) nanowire bundles, D) EDAX spectrum of nanowire bundles. The insets are the corresponding high-resolution TEM images.

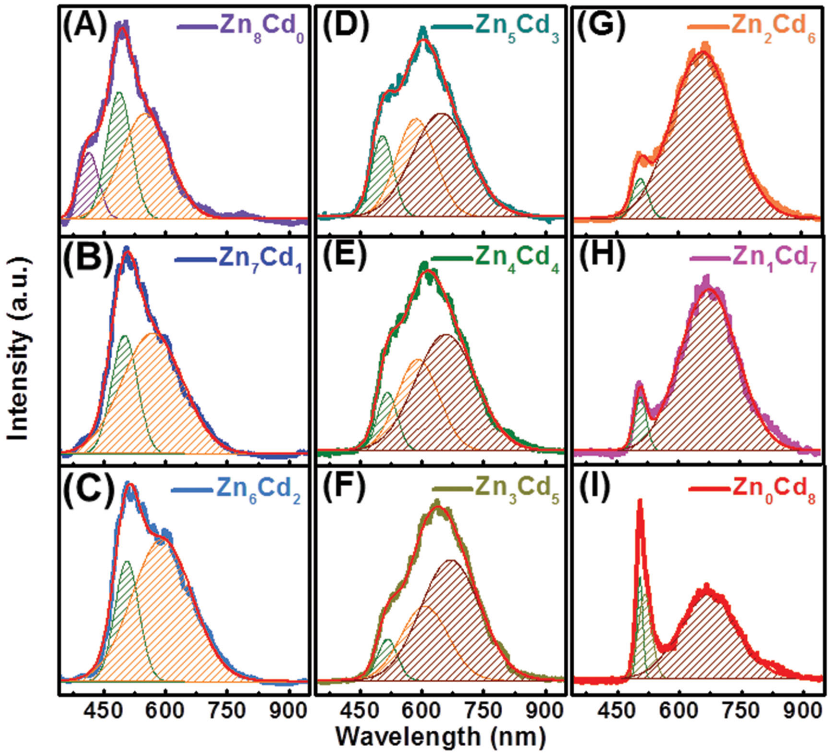

Figure 4. Photoluminescence spectra of Zn_mCd_n under excitation of 325 nm laser.

are lower than those (515 and 620 nm) in Wang' s report. They could be assigned the transition from the interstitial metal state to valence band and sulfur vacancies to valence band, respectively.

In the case of Zn_7Cd_1 (Figure 4B), the blue emission band at 410 nm rapidly deceases, and the bands at 480 and 560 nm obviously shift to high wavelength 500 and 600 nm, respectively. The red shift of emission bands could be also attributed to formation of solid solution due to the addition of Cd. For the PL spectra of Zn_0Cd_8 sample (Figure 4I), there are a sharp emission band at ≈505 nm and a broad band at 670 nm. The peak at 505 nm can be fitted into 2 PL band at 505 and 515 nm. Normally, the former is attributed to the intrinsic emission of CdS and the latter is assigned to the surface state of CdS.[12] The PL band at 670 nm is contributed from defects, such as sulfur vacancies, of CdS.[12,13] In the case of Zn_1Cd_7 solid solution sample (Figure 4H), the emission band at 515 nm rapidly decreases, and the emission band at 670 nm slightly blue shift, which can be attributed to the formation of solid solution. The PL spectrum of Zn_4Cd_4 (Figure 4E) contains three broad emission bands at 515, 589, and 656 nm. Because the Zn_4Cd_4 contains two kinds of solid solutions: $Zn_{0.31}Cd_{0.69}S_{0.77}$ and $Zn_{0.78}Cd_{0.22}S_{0.78}$. The emission band at ~ 515 nm can be attributed to the surface states of both solid solutions and the sulfur vacancies emission of $Zn_{0.31}Cd_{0.69}S_{0.77}$ may contribute to emission band at ≈656 nm, the emission band at ≈589 nm may be assigned to the defects of $Zn_{0.78}Cd_{0.22}S_{0.78}$. The emission of as-prepared Zn_mCd_n samples mainly stem from defects on the surface of solid solutions.

2.4. X-Ray Photoelectron Spectroscopy

X-ray photoelectron spectroscopy (XPS) is employed to further verify the valence state of Zn and Cd in the samples. **Figure 5**A shows the high-resolution Cd 3d XPS spectra of Zn_0Cd_8, Zn_4Cd_4, and Zn_4Cd_4 etched with electron beam. In the case of Zn_0Cd_8 (CdS) and Zn_4Cd_4 samples, two peaks at ≈411.5 and ≈405.0 eV are contributed from Cd $3d_{3/2}$ and $3d_{5/2}$, respectively. Each Cd 3d XPS peak can be derived into two Gaussian peaks, 411.5 and 412.5 eV for Cd $3d_{3/2}$ peak and 404.7 and 405.7 eV for Cd $3d_{5/2}$ peak, respectively. Normally, the binding energies corresponding to Cd $3d_{3/2}$ and $3d_{5/2}$ for divalent cadmium (Cd^{2+}) appear at 411.8 and 405.3 eV for CdS, respectively.[10,14] We deduce that the high binding energy peaks (412.5 and 405. 7 eV) can be assigned to Cd $3d_{3/2}$ and $3d_{5/2}$ of Cd^{2+} in Zn_0Cd_8. According to the previous reports, the binding energy of Cd^0 3d locates at 410.7 and 404.1 eV for $3d_{3/2}$ and $3d_{5/2}$.[15] In the high resolution Cd 3d XPS spectra, the XPS components at low bonding energy (411.5 and 404.7 eV) could be assigned to Cd $3d_{3/2}$ and $3d_{5/2}$ of Cd in low valence state or interstitial Cd. Similarly, two sets of XPS peaks appear in the Cd 3d XPS spectra of Zn_4Cd_4 sample. The high binding energy XPS peaks at 412.6 and 406.0 eV are attribute to Cd $3d_{3/2}$ and $3d_{5/2}$ of Cd^{2+} and the XPS signals at low binding energy (411.7 and 404.9 eV) are assigned to the Cd $3d_{3/2}$ and $3d_{5/2}$ of low valence Cd in Zn_4Cd_4 solid solution. Based on the above analysis, we infer that low valence Cd and Cd^{2+} state coexist in the as-prepared Zn-Cd-S solid solutions. Although low valence Cd is detected in the XPS spectra, no metallic Cd signal is observed in the XRD pattern (Figure 1) of any Zn_mCd_n sample. We deduce that XPS signal of low valence Cd may contribute from the interstitial Cd on the top surface of the as-prepared sample due to the reaction carried out in the hydrazine media. Electron beam etching was performed on the Zn_4Cd_4 sample in the XPS measurement. The Cd 3d XPS profile at a depth of 60 nm is shown in top plot of Figure 5A. Only two peaks at 405.5 and 412.3 eV are observed. These peaks contributed from the Cd^{2+} in the Zn-Cd-S solid solution. That indicates that the valence states of Cd are divalent inside of the solid solution, low valence state Cd only exists on the top surface of solid solution.

Similar as Cd 3d XPS spectra, high resolution Zn 2p XPS spectra of Zn_8Cd_0 (ZnS), Zn_4Cd_4 and Zn_4Cd_4 etched with electron beam samples display two peaks at ≈1020 and 1043 eV (Figure 5B) contributing from Zn $2p_{3/2}$ and $2p_{1/2}$. In the cases of Zn_8Cd_0 and Zn_4Cd_4, the Zn $2p_{3/2}$ and $2p_{1/2}$ peaks can also be fitted into two Gaussian peaks for each, respectively. The high binding energy peaks at 1022.7 and 1045.9 eV belong to Zn $2p_{3/2}$ and $2p_{1/2}$ for the divalent Zn in the Zn_8Cd_0 (ZnS), and the peaks at 1022.6 and 1045.7 eV are assigned to the Zn $2p_{3/2}$ and $2p_{1/2}$ of Zn^{2+} in the Zn_4Cd_4 solid solution.[10] The peaks at relative low binding energy (1020.3 and 1043.9 eV for Zn_8Cd_0 and 1020.5 and 1043.6 eV for Zn_4Cd_4) are contributed from the low valence state Zn in metal state.[16] These results further confirm that the defects such as interstitial Zn and low valence Zn exist in the as-prepared solid solution samples prepared from hydrazine. The high resolution Zn 2p XPS spectra of Zn_4Cd_4 at a depth of 60 nm clearly show two high binding energy peaks at 1022.3 and 1045.3 eV, which are assigned to the Zn^{2+} in the solid solution. Based on the above XPS results, we propose that the metals in the solid solutions are divalent state inside of Zn_mCd_n samples covered with rich defects, such as sulfur vacancies, interstitial metal, and metals in low valence state.

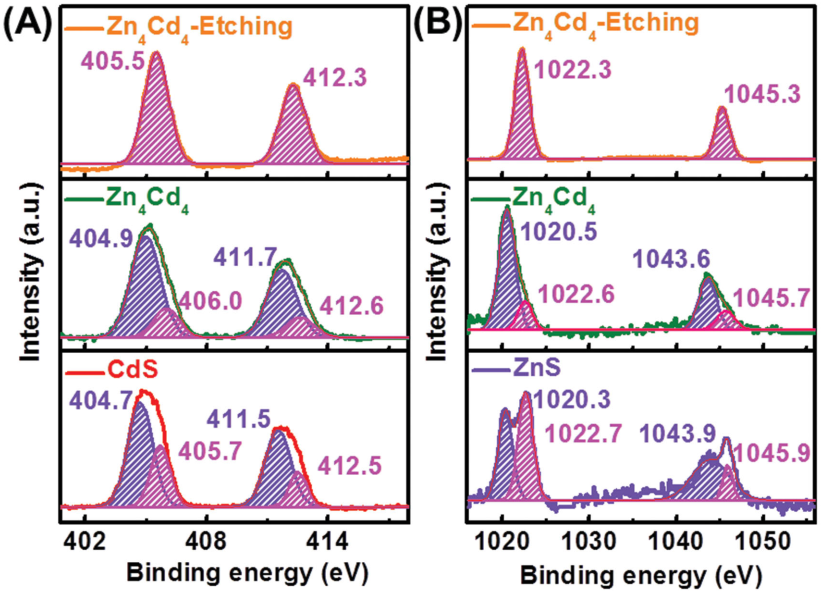

Figure 5. High resolution X-ray photoelectron spectroscopy (XPS) of Zn_0Cd_8, Zn_4Cd_4, and Zn_8Cd_0. A) Cd 3d XPS spectra of Zn_0Cd_8 (bottom), Zn_4Cd_4 (middle), and Zn_4Cd_4 etched with electron beam at depth of 60 nm (top), B) Zn 2p XPS spectra of Zn_8Cd_0 (bottom), Zn_4Cd_4 (middle), and Zn_4Cd_4 etched with electron beam at depth of 60 nm (top).

Based on the results of EDAX, XPS, and PL spectra, we can deduce that defects, such as sulfur vacancies, interstitial metal, and Zn and Cd in low valence state, coexist in the surface of solid solutions prepared in the hydrazine.

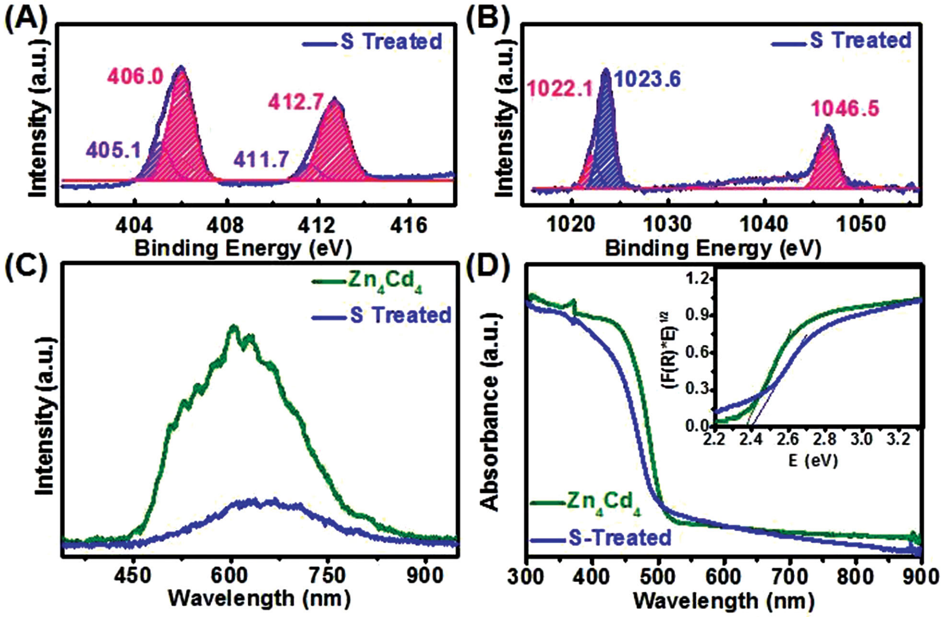

Figure 6. Comparison of the A) Cd 3d and B) Zn 2p XPS, C) PL emission, D) UV–vis absorption spectra and Tauc plots (inset of D) of Zn_4Cd_4 and Zn_4Cd_4 treated with sulfur vapor at 500 °C for 5 h.

2.5. Sulfurization of Zn-Cd-S Solid Solution

In order to investigate the effect of defects on the photocatalytic performance of Zn-Cd-S solid solutions, Zn_4Cd_4 sample was treated with sulfur vapor under Ar environment at 500 °C for 5 h to remove the surface defects. Figure S8 of the Supporting Information shows the XRD of Zn_4Cd_4 sample before and after sulfur vapor treatment. No obvious change was observed for crystalline phase. The high resolution XPS spectra of Cd 3d and Zn 2p (**Figure 6**A,B) display that the reduction of the fraction of low binding energy component and the increase of high binding energy compared with as-prepared Zn_4Cd_4 sample (Figure 5). That implies the surface defects, such as sulfur vacancies and interstitial metal, dramatically decrease after the sulfur vapor treatment. The PL emission of Zn_4Cd_4 mainly contributes from the surface defects. After sulfur vapor treatment, the PL spectra exhibit a significant PL quenching (Figure 6C), further indicating the decrease of surface defects, as well. As we know, the existence of defect band results in narrowing the band gap of semiconductor because defect band will appear between conduction band and valence band. On the contrary, the band gap is expected to slightly enlarge when the defects are removed. A blue-shift is also observed in the UV–vis absorption spectra (Figure 6D). The optical absorption properties of other Zn_mCd_n samples are shown in Figures S9–S11 of the Supporting Information. All these results demonstrate that sulfur vapor treatment can effectively remove the surface defects of Zn-Cd-S solid solution.

2.6. Photocatalytic Activity

Usually, photocatalysts with higher specific surface areas are beneficial for the enhancement of photocatalytic performance. Thus, the BET surface areas and pore structures of the as-prepared samples were investigated by the nitrogen adsorption–desorption measurement. The N_2 adsorption–desorption isotherm of the Zn_4Cd_4 photocatalysts, as depicted in Figure S11 of the Supporting Information, shows that the specific surface area is ≈90 m^2 g^{-1} for Zn_4Cd_4. The isotherms show high adsorption at a high relative pressure (P/P_0) range from 0.8 to 1.0, suggesting the formation of large mesopores and macropores. The mesopores and macropore may be from the nanorods and aggregates stacking, respectively. The pore size distribution curve (inset of Figure S11, Supporting Information) displays a peak below 5 nm and a wide range of 5–50 nm, confirming the coexistence of mesopores and macropores.

Photocatalytic H_2 production activities of as-prepared Zn_mCd_n solid solutions were evaluated under visible light ($\lambda > 420$ nm) irradiation and using Na_2S and Na_2SO_3 mixed aqueous solution as the sacrificial reagent without Pt as cocatalyst. It was expected that high photocatalytic performance could be achieved for the Zn_mCd_n photocatalyst prepared from hydrazine hydrothermal route due to the existence of defects. Firstly, $Zn_{0.5}Cd_{0.5}S$ is synthesized by similar synthesis route using H_2O as solvent and shows ≈30 µmol h^{-1} (≈1.2 mmol h^{-1} g^{-1}) for 25 mg photocatalyst under visible light irradiation. **Figure 7**A shows the comparison of the average visible light photocatalytic H_2 production rate of Zn_mCd_n samples and sulfur vapor treated Zn_4Cd_4. The Zn_8Cd_0 sample shows a negligible visible light photocatalytic activity due to no absorption in the visible region of ZnS. When the Cd is introduced and forms Zn-Cd-S solid solution, the photocatalytic activity dramatically increase to ≈200 mmol h^{-1} for 50 mg Zn_7Cd_1 sample, which is related to the big red-shift in the UV–vis spectra. The extension of light absorption is the main contributor for the photocatalytic H_2 production. With the increase of Cd amount, the absorption band edge of solid solution is further red shift. The H_2 production rate of Zn_mCd_n gradually increases with the addition of Cd and

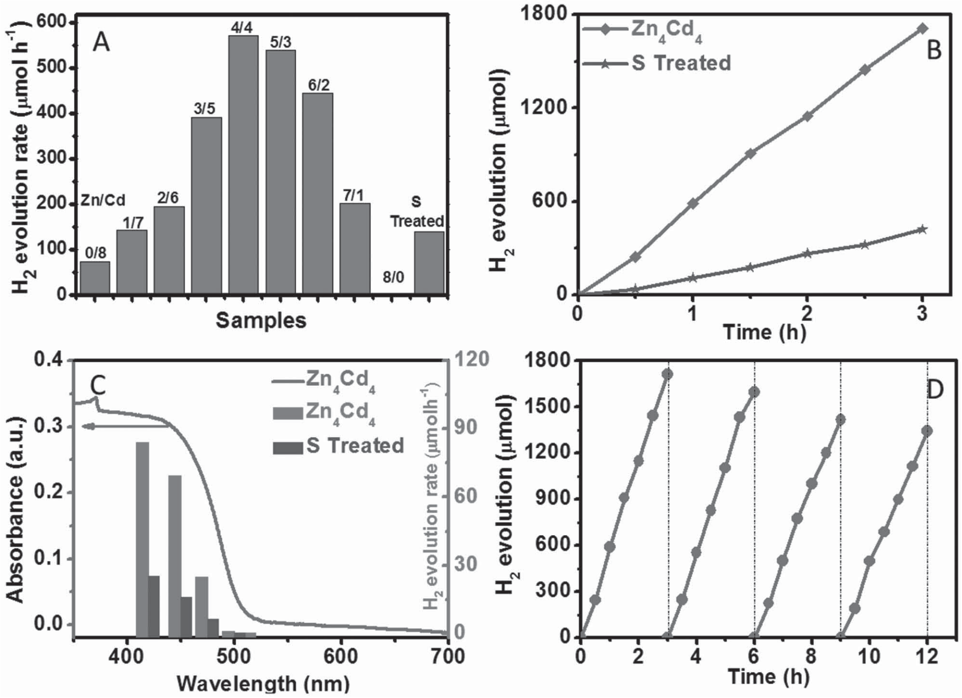

Figure 7. A) Photocatalytic H$_2$ production rate from 0.35 m Na$_2$S and 0.35 m Na$_2$SO$_3$ mixed aqueous solution of 50 mg Zn$_m$Cd$_n$ and S vapor treated Zn$_4$Cd$_4$ under visible light ($\lambda > 420$ nm) irradiation. B) Comparison of the time dependence photocatalytic activities of Zn$_4$Cd$_4$ samples and S vapor treated Zn$_4$Cd$_4$ sample for the photocatalytic H$_2$ production under visible light ($\lambda > 420$ nm) irradiation. C) The wavelength dependence of photocatalytic H$_2$ production rate for Zn$_4$Cd$_4$ and Zn$_4$Cd$_4$ treated with sulfur vapor. D) Recycling measurements of H$_2$ production through photocatalytic water splitting with Zn$_4$Cd$_4$ under visible light ($\lambda > 420$ nm) irradiation.

up to 571 μmol h^{-1} for 50 mg Zn$_4$Cd$_4$ (≈11.4 mmol h^{-1} g^{-1}). A further increase in the Cd content in the Zn$_m$Cd$_n$ solid solutions resulted in a decrease of the photocatalytic activity. The Zn$_0$Cd$_8$ exhibits a low photocatalytic activity with a H$_2$ production rate of 73 μmol h^{-1} for 50 mg photocatalyst (≈1.46 mmol h^{-1} g^{-1}). A balance between the light absorption capacity and the reduction power in the Zn$_4$Cd$_4$ sample probably leads to a higher efficiency of visible-light photocatalytic H$_2$ production than that of the ZnS and CdS samples.[10] The Zn$_4$Cd$_4$ sample treated with sulfur vapor exhibits a moderate H$_2$ evolution rate of 140 μmol h^{-1} for 50 mg photocatalyst (≈2.8 mmol h^{-1} g^{-1}), which is about four times lower than that of as-prepared Zn$_4$Cd$_4$ sample (Figure 7B). These demonstrate that the Zn-Cd-S solid solution with defects exhibit better photocatalytic performance than that without defects.

Figure 7C displays the wavelength dependence of photocatalytic H$_2$ production rate for as-prepared Zn$_4$Cd$_4$ and Zn$_4$Cd$_4$ treated with sulfur vapor. The active wavelength of Zn$_4$Cd$_4$ reaches 520 nm and its corresponding apparent QE at 420 ± 10 nm reaches 16.9%. However, the active wavelength of sulfur vapor treated Zn$_4$Cd$_4$ only reaches 500 nm and the apparent QE is about 5.1% at 420 ± 10 nm. These further confirm that Zn-Cd-S solid solution with surface defects has narrower band gap and high efficient charge separation. In addition, the Zn$_4$Cd$_4$ sample exhibits much better H$_2$ evolution rate within the whole absorption band than sulfur treated Zn$_4$Cd$_4$ sample. These results not only convincingly show that the photocatalytic activity of Zn$_4$Cd$_4$ matches the optical absorption, but also shows a stable improvement in the H$_2$ production of Zn$_4$Cd$_4$ over the whole range of optical activities from UV to visible light region. The stability of Zn-Cd-S solid solution was carried out for the Zn$_4$Cd$_4$ sample. After 4 cycles test, the photocatalytic H$_2$ production rate has a slight decrease (≈21.7%, Figure 7D), which is a general challenge for the sulfide photocatalyst.

2.7. Theoretical Calculations

In order to understand the effect of defects on the electronic properties of Zn-Cd-S solid solutions, theoretical models have been constructed to mimic the Zn-Cd-S with sulfur vacancy. All the models were calculated by using first-principles density function theory (DFT) with the VASP package.[17] The projected-augmented wave (PAW) approach was applied to treat the ion–electron interactions.[18] The exchange-correlation energy of electrons was described in the generalized gradient approximation (GGA) with the functional parameterization of PBE.[19] The energy cut-off was set at 400 eV, and a criterion of at least 0.0001 eV per atom was placed on the self-consistent convergence of the total energy.

Due to that the content of Zn and Cd in as-prepared Zn-Cd-S solid solutions is not equal even in the case of Zn$_4$Cd$_4$, Zn$_{0.375}$Cd$_{0.625}$S and Zn$_{0.75}$Cd$_{0.25}$S (for nanorod aggragates and nanowire bundles, respectively) are chosen as example to calculate the DOS (density of state) of solid solution. Zn$_{0.375}$Cd$_{0.625}$S$_{0.933}$ and Zn$_{0.75}$Cd$_{0.25}$S$_{0.933}$ stand for the corresponding sulfur vacancy states, and all the calculations were carried out with the 2 × 2 × 2 supercells. In order to compare the energy levels of Zn$_{0.375}$Cd$_{0.625}$S and Zn$_{0.375}$Cd$_{0.625}$S$_{0.933}$,

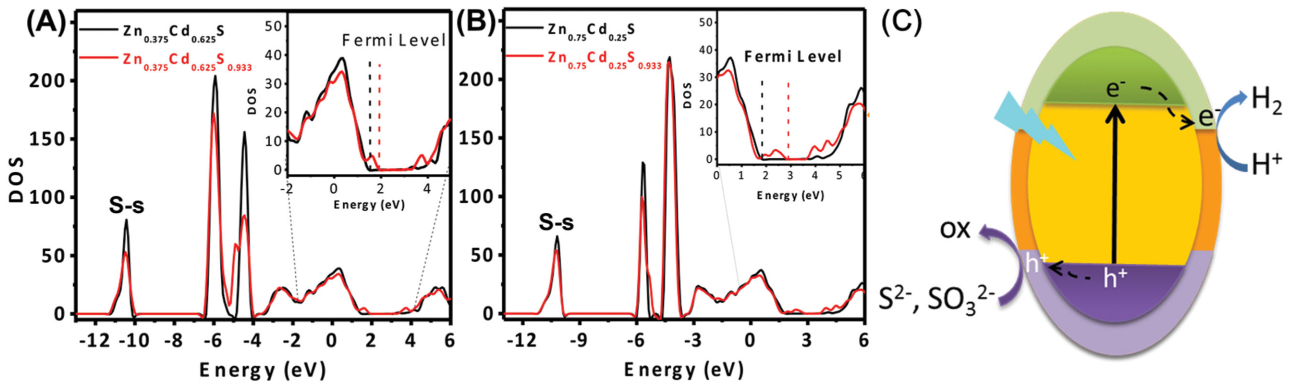

Figure 8. DFT calculated band structure of A) $Zn_{0.375}Cd_{0.625}S$ and B) $Zn_{0.75}Cd_{0.25}S$, and C) defect-assisted mechanism of photocatalytic water splitting.

the S–s states, whose energy level is almost stable for the slightly different chemical environment, are specified at the same energy value (–11.5 eV). After the sulfur vacancies were introduced into $Zn_{0.375}Cd_{0.625}S$, as shown in **Figure 8**A, two defect energy states in the DOS of $Zn_{0.375}Cd_{0.625}S_{0.933}$ appear at above the valence band maximum (VBM) and below the conductor band minimum (CBM), respectively. That imply that both VB and CB of $Zn_{0.375}Cd_{0.625}S$ are altered at the same time and the band gap is narrowed due to the introduction of sulfur vacancy. Similarly, the VB and CB of $Zn_{0.75}Cd_{0.25}S$ are also changed, when the sulfur vacancies were induced, the DOS around the Fermi level is significantly reformed, and the band gap is also reduced. It is undoubtedly that the S vacancies reform the electronic structure of the Zn-Cd-S solid solution, and adjusts the band gap to a smaller value.

On the basis of the above experimental and theoretical results, the influence of defects on the photocatalytic activity of Zn-Cd-S solid solution is proposed as the following defect-assisted mechanism (Figure 8C). According to the theoretical calculation, the surface defects result in the formation of defect energy band located below the conductin band and/or above the valance band. These surface defects can effectively capture the photogenerated charges, promote charge transfer from inside to the surface and prevent from charge recombination, as well. These factors greatly promote charge separation and transfer process in the whole photocatalytic reaction. Overall, the photocatalytic activity is enhanced by the introduction of defects on the surface of Zn-Cd-S solid solution.

3. Conclusion

In summary, we developed a simple one-step hydrothermal route in the hydrazine media to fabricate visible-light active Zn-Cd-S solid solutions with surface defects for photocatalytic H_2 evolution. The electron microscopy images and XRD result disclose that the as-prepared Zn-Cd-S solid solutions contain two kinds of solid solutions (nanorod aggregates and nanowire bundles). EDAX, PL, and XPS results confirm the existence of surface defects, such as sulfur vacancies, interstitial metal, and metal in low valence state on the top surface of nanostructure. UV–vis, PL, and XPS spectra further confirmed that the surface defects could be removed by the treatment. Comparing with defect free solid solution, the as-prepared Zn_4Cd_4 exhibit wider visible light absorption range and higher H_2 production rate over the whole optical absorption band at each wavelength. Overall visible-light H_2 production rate of as-prepared Zn_4Cd_4 is about fourfold better than that of defect free solid solution. Theoretical calculation results imply that defect bands appear at both blow CB and above VB of solid solution, which result in a narrow band gap surface layer. Surface defects promote the photogenerated charges easily transfer from inside toward surface of nanostructure. That is beneficial for the photocatalytic reaction happened on the surface of photocatalyst. Our results may shed a light on the design of visible light photocatalyst in the future.

4. Experimental Section

Chemicals and Materials: $Zn(OAc)_2 \cdot 2H_2O$ and $Cd(OAc)_2 \cdot 2H_2O$ were purchased from Sinopharm Chemical Reagent Company. Thiourea was purchased from Tianjin Tiantai Chemical Reagent Company. Hydrazine hydrate (80%), $Na_2S \cdot 9H_2O$ and Na_2SO_3 were purchased from Tianjin Guangfu Technology Development Company. All chemicals were reagent grade and used without further purification.

Preparation of Zn-Cd-S Solid Solutions: In a typical synthesis, 1 mmol $Zn(OAc)_2 \cdot 2H_2O$ and $Cd(OAc)_2 \cdot 2H_2O$ with different molar ratio (0-8/8-0), and 2 mmol thiourea were dissolved in 30 mL hydrazine hydrate. The total amount of $Zn(OAc)_2$ and $Cd(OAc)_2$ is 1 mmol. The solution was constantly stirred for 20 min at room temperature and then transferred into 50 mL Teflon-lined stainless steel autoclave. Afterward, the autoclave was sealed and maintained at 180 °C in an electric oven for 24 h, and then naturally cool to room temperature. The as-prepared precipitate was collected by centrifugation, washed with deionized water and ethanol for three times, respectively. Finally, the precipitate was dried in a 70 °C oven over 10 h.

Preparation of Zn-Cd-S Solid Solution Treated with Sulfur Vapor: The as-prepared Zn_4Cd_4 sample and sulfur powder were placed in an porcelain boat covered by an aluminum foil and subsequently heated to 500 °C in a tube furnace for 5 h at a heating rate of 5 °C min^{-1} under argon flow, and then cool to room temperature naturally. The product was washed with CS_2 and ethanol for several times to remove excess sulfur, and finally dried in a 70 °C oven for 5h.

Characterizations: The crystalline structure was measured by using a Bruker AXS D8 Focus X-ray diffractometer, using Cu Kα radiation ($\lambda = 1.54056$ Å). Scanning electron microscopy (SEM) images and EDAX were measured on a JEOL JSM 4800F. TEM analyses were performed on a FEI Tecnai G^2 F20 field emission electron microscope with an accelerating voltage of 200 kV. The UV–vis absorption spectra (converted from diffuse reflectance spectra) were recorded on a Shimadzu UV-3600 UV/vis–NIR scanning spectrophotometer. X-ray photoelectron spectroscopy (XPS) analyses were performed on a Thermo Scientific ESCALAB 250 Multitechnique Surface Analysis. The Brunauer–Emmett–Teller (BET) specific surface area was measured using a Mictomeritics Gemini V Surface Area and Pore Size Analyzer. The photoluminescence spectra (PL) measurement was conducted by LabRam infinity (Jobin Yvon Horiba) spectrophotometer with a 325 nm IK series He-Cd Laser.

Photocatalytic Activities: The photocatalytic activity of the samples for water splitting was evaluated by monitoring the generated H2. The measurement was carried out in the equipment of Labsolar-III AG system supplied by Beijing Perfectlight Technology Co., Ltd. In a typical procedure, 50 mg of photocatalyst was dispersed into 80 mL aqueous solution of 0.35 m Na_2SO_3 and 0.35 m Na_2S in a closed gas circulation system. The visible light irradiation was obtained from a 300 W Xe lamp (Perfect Light Commpany Solaredge700) with an UVCUT-420 nm filter (Newport). The amount of generated H_2 was determined by an online gas chromatography (Schimazu GC-2014) with thermal conductivity detector (TCD).

Supporting Information

Supporting Information is available from the Wiley Online Library or from the author.

Acknowledgements

The authors thank the National Natural Science Foundation of China (21301166, 61361166004, and 61176016) and the Science and Technology Department of Jilin Province (20130522127JH). Z.S. is grateful for support from the Beijing High-level Talent Program. This work was supported by the open research fund program of the State Key Laboratory of Luminescence and Applications (Changchun Institute of Optics, Fine Mechanics and Physics, CAS).

[1] a) X. Chen, A. Selloni, *Chem. Rev.* **2014**, *114*, 9281; b) K. S. Joya, Y. F. Joya, K. Ocakoglu, R. van de Krol, *Angew. Chem., Int. Ed.* **2013**, *52*, 10426; c) K. Zhang, L. Guo, *Catal. Sci. Technol.* **2013**, *3*, 1672.
[2] T. Takata, K. Domen, *J. Phys. Chem. C* **2009**, *113*, 19386.
[3] N. Serpone, D. Lawless, J. Disdier, J.-M. Herrmann, *Langmuir* **1994**, *10*, 643; b) W. Shockley, W. T. Read, *Phys. Rev.* **1952**, *87*, 835.
[4] a) A. Ananthanarayanan, Y. Wang, P. Routh, M. A. Sk, A. Than, M. Lin, J. Zhang, J. Chen, H. Sun, P. Chen, *Nanoscale* **2015**, *7*, 8159; b) X. Pan, M.-Q. Yang, X. Fu, N. Zhang, Y.-J. Xu, *Nanoscale* **2013**, *5*, 3601.
[5] a) F. Zuo, L. Wang, T. Wu, Z. Zhang, D. Borchardt, P. Feng, *J. Am. Chem. Soc.* **2010**, *132*, 11856; b) F. Zuo, K. Bozhilov, R. J. Dillon, L. Wang, P. Smith, X. Zhao, C. Bardeen, P. Feng, *Angew. Chem., Int. Ed.* **2012**, *51*, 6223; c) K. Xie, N. Umezawa, N. Zhang, P. Reunchan, Y. Zhang, J. Ye, *Energy Environ. Sci.* **2011**, *4*, 4211; d) Z. Zheng, B. Huang, X. Meng, J. Wang, S. Wang, Z. Lou, Z. Wang, X. Qin, X. Zhang, Y. Dai, *Chem. Commun.* **2013**, *49*, 868; e) B. Santara, P. K. Giri, K. Imakita, M. Fujii, *Nanoscale* **2013**, *5*, 5476; f) C. Zhou, Y. Zhao, L. Shang, Y. Cao, L.-Z. Wu, C.-H. Tung, T. Zhang, *Chem. Commun.* **2014**, *50*, 9554.
[6] H. Tan, Z. Zhao, M. Niu, C. Mao, D. Cao, D. Cheng, P. Feng, Z. Sun, *Nanoscale* **2014**, *6*, 10216.
[7] P. Niu, L.-C. Yin, Y.-Q. Yang, G. Liu, H.-M. Cheng, *Adv. Mater.* **2014**, *26*, 8046.
[8] J. Shi, H. n. Cui, Z. Liang, X. Lu, Y. Tong, C. Su, H. Liu, *Energy Environ. Sci.* **2011**, *4*, 466.
[9] a) L. Wang, W. Wang, M. Shang, W. Yin, S. Sun, L. Zhang, *Int. J. Hydrogen Energy* **2010**, *35*, 19; b) M. Liu, L. Wang, G. Lu, X. Yao, L. Guo, *Energy Environ. Sci.* **2011**, *4*, 1372; c) J. Ran, J. Zhang, J. Yu, S. Z. Qiao, *ChemSusChem* **2014**, *7*, 3426.
[10] Q. Li, H. Meng, P. Zhou, Y. Zheng, J. Wang, J. Yu, J. Gong, *ACS Catal.* **2013**, *3*, 882.
[11] L. Wang, Y. Zheng, X. Li, W. Dong, W. Tang, B. Chen, C. Li, X. Li, T. Zhang, W. Xu, *Thin Solid Films* **2011**, *519*, 5673.
[12] J. J. Ramsden, M. Gratzel, *J. Chem. Soc., Faraday Trans. 1* **1984**, *80*, 919.
[13] a) Y. T. Sihvonen, D. R. Boyd, C. D. Woelke, *Phys. Rev.* **1959**, *113*, 965; b) A. A. Vuylsteke, Y. T. Sihvonen, *Phys. Rev.* **1959**, *113*, 40.
[14] J. Pan, G. Liu, G. Q. M. Lu, H. M. Cheng, *Angew. Chem., Int. Ed.* **2011**, *50*, 2133.
[15] a) Q. Wang, J. Li, Y. Bai, J. Lian, H. Huang, Z. Li, Z. Lei, W. Shangguan, *Green Chem.* **2014**, *16*, 2728; b) R. D. Seals, R. Alexander, L. T. Taylor, J. G. Dillard, *Inorgan. Chem.* **1973**, *12*, 2485.
[16] a) D. Chadwick, T. Hashemi, *Corros. Sci.* **1978**, *18*, 39; b) N. T. Mai, T. T. Thuy, D. M. Mott, S. Maenosono, *CrystEngComm* **2013**, *15*, 6606.
[17] G. Kresse, J. Furthmüller, *Comput. Mater. Sci.* **1996**, *6*, 15.
[18] P. E. Blöchl, *Phys. Rev. B* **1994**, *50*, 17953.
[19] J. P. Perdew, K. Burke, M. Ernzerhof, *Phys. Rev. Lett.* **1996**, *77*, 3865.

Received: October 11, 2015
Revised: November 9, 2015